J. Fluid Mech. (2006), *vol.* 559, *pp.* 307–334.
doi:10.1017/S0022112006000474 Printed in the United Kingdom

Effect of buoyancy on the dynamics of a turbulent boundary layer laden with microbubbles

By A. ALISEDA AND J. C. LASHERAS

Department of Mechanical and Aerospace Engineering, University of California San Diego, La Jolla, CA 92093, USA

(Received 1 March 2005 and in revised form 26 December 2005)

This paper describes the effect of gravity on the dynamics of a turbulent boundary layer laden with microbubbles. A poly-dispersed distribution of air bubbles with diameters in the 5–1000 μm range was injected at the leading edge of a surface-piercing vertical flat plate. Reynolds numbers, based on the momentum thickness, up to 2000 and bubble void fractions up to 5 % were studied. The streamwise velocity profile was found to satisfy the logarithmic law characteristic of single-phase turbulent boundary layers, for the range of bubble void fractions studied. It was found that the effect of the bubbles could be modelled as an offset from the wall which increases as the bubble void fraction is increased. Bubbles were observed to segregate by size within the boundary layer, giving rise to strong inhomogeneities in the local void fraction. Buoyancy acting on this region of high bubble void fraction leads to a strongly sheared vertical velocity profile, which divides the boundary layer into three subregions: an inner region closest to the wall populated by very small bubbles with low vertical velocity; an intermediate region where large bubbles accumulate, and which also had the largest number density, resulting in a large vertical velocity induced by the buoyancy; and an outer region with significantly fewer bubbles than the two previously described and of smaller diameters. These three regions correlated well with the presence of a secondary flow normal to the wall in which the wall-normal velocity was positive in the inner region (fluid moved away from the wall), went through zero in the intermediate region (where the vertical velocity reached its maximum) and was negative in the outer region (fluid moved towards the wall). This secondary flow was found to depend strongly on the bubble void fraction and did not scale well with the viscous scales of the boundary layer.

1. Introduction

Turbulent multiphase flows have direct relevance in many industrial and environmental processes. Those processes, including heat exchange in nuclear reactors and gas exchange between the ocean and the atmosphere, often involve a dense fluid as the turbulent carrier flow and a dilute concentration of gas bubbles as the disperse phase.

The study of the interaction of turbulence with a dispersed phase has a long and illustrious history, starting with the theory of turbulent dispersion by Taylor (1921). However, for many years such theories treated turbulence as a random source for agitation of the particles. It was not until the last few decades that the necessary tools made it possible to study in detail the many intriguing phenomena that characterize

this type of flow. Whereas the dispersion of particles by turbulent flows and their common interactions have been thoroughly studied (Crowe, Chung & Troutt 1988; Eaton & Fessler 1994), the literature on bubbly turbulent flows is quite sparse.

Experimental investigation of turbulent bubbly flows has been mostly carried out with relatively large bubbles and volume fractions. Lance & Bataille (1991) studied the turbulence characteristics of the continuous phase in an upwards flowing water channel, where turbulence was introduced both by a grid and by ellipsoidal bubbles with an equivalent diameter of 5 mm, approximately equal to the Taylor microscale of the single-phase flow. As the bubble void fraction was increased from 0 to 5 %, the flow transitioned from a regime where the hydrodynamic interaction of the bubbles was negligible to one in which the bubbles transfered a large amount of kinetic energy to the flow, modifying the one-dimensional spectra from the classical $-5/3$ power law to a $-8/3$ dependency. Panidis & Papailiou (2000) revisited the problem of bubbles injected into an upward-moving grid-induced turbulent water flow. They focused on the bubble spatial distribution, as well as on the effect of the bubbles on the underlying carrier-flow turbulence. They found a non-uniform distribution of the bubbles, with a peak in the local void fraction located approximately halfway between the channel wall and the centreline. An associated peak in the streamwise velocity was also reported, presumably induced by the stronger buoyancy of the bubbles at the location of the void fraction peak. The reasons for the existence and location of these peaks were not provided and several mechanisms, such a lift due to the interaction with the mean shear (Segre & Silberberg 1962), or preferential accumulation by large eddies (Rightley & Lasheras 2000), were suggested as possible. Because in these experiments the bubbles were several millimetres in diameter and the volume fraction was very high ($\approx 5\,\%$), the effect of the carrier flow on the dynamics of the bubbles was not satisfactorily analysed. Moreover, because the mean flow was in the same direction as gravity, the rise velocity was not considered. Sridhar & Katz (1995) carried out experiments to determine the forces acting on bubbles in the 500–800 μm range due to non-uniform flow. They found drag coefficients that agreed well with steady-state data and lift coefficients that did not agree with existing theoretical or numerical models. In the course of their experiments they measured the trajectory of a bubble entrained by a laminar vortex and were able to reproduce it with calculations using the equation of motion from Maxey & Riley (1983), with adequate coefficients. Rightley & Lasheras (2000) studied the dispersion of microbubbles in a free shear layer. Using bubbles with diameters smaller than 100 μm so that their rise velocity was negligible, they were able to characterize the effect of the large coherent vortices present in a mixing layer on the bubble dispersion. Poorte & Biesheuvel (2002) reported experimental evidence of a decrease in the rise velocity of bubbles caused by homogeneous isotropic turbulence, created by an active grid.

Numerical simulations of the interaction of bubbles with a vorticity field were carried out by Maxey and collaborators. In Wang & Maxey (1993*b*), they reported preferential accumulation of bubbles in homogeneous isotropic turbulence. In parallel with their simulations of heavy particles, they confirmed the intuition that microbubbles would be subject to the same accumulation effect due to turbulence, except that, because the density ratio is inverted, accumulation of bubbles occurs in regions of very high vorticity. It took several years, however, to report the equivalent study for the rise velocity of the bubbles. Counter to what happens with heavy particles, bubbles have their rise velocity reduced by the turbulence. Maxey *et al.* (1997) found that the interaction with the turbulence reduced the rise velocity of the bubbles because of the increased residence time of the bubbles in the downward side

of the eddies, where there is a theoretical static equilibrium point (Tio *et al.* 1993). This is because instead of being driven by inertia to the downward convergence zones between eddies, they are driven to the eddies cores, where pressure forces oppose the rising that would take them away from these regions. Spelt & Biesheuvel (1997) also found these effects in their simulations of bubbles in a vortical flow with a turbulence-like spectrum. Direct numerical simulations (DNS) of bubbly turbulent flows have been performed by Druzhinin & Elghobashi (1998), who found that preferential accumulation is not significant for very small bubbles in low-Reynolds-number homogeneous, isotropic, decaying turbulence. Under these circumstances the effect of the bubbles is similar to stratification, enhancing the turbulence decay for stable stratification and delaying it in the unstable case. Mazzitelli, Lohse & Toschi (2003) reported the results of a DNS study of microbubbles in homogeneous isotropic turbulence. They focused attention on the effect of lift force and found that bubbles increase their residence time in the downward side of the eddies, thus reducing the bubble mean rise velocity. Large-scale velocity fluctuations in the carrier fluid are inhibited by the buoyancy, while energy is added at the small scales of the turbulence, resulting in a net reduction of the turbulence decay rate.

The interaction of bubbles with a turbulent boundary layer has been studied experimentally by Moursali, Marie & Bataille (1995) and Marie, Moursali & Trang-Cong (1997). They introduced large ellipsoidal bubbles (3.5–6 mm diameter) at the leading edge of a vertical flat plate and measured the void fraction distribution as the boundary layer developed. They found that larger bubbles flow away from the wall, while smaller bubbles remain inside the boundary layer, with the void fraction peaking at a distance from the wall slightly larger than the bubble radius. Merkle & Deutsch (1992) studied the behaviour of small spherical bubbles introduced in a flat-plate turbulent boundary layer. They determined that the bubbles tend to diffuse throughout the boundary layer. Unfortunately, the focus of the experiment was drag reduction due to the bubble injection. Accordingly, a very large void fraction was introduced and the information pertaining to the bubbles was only qualitative. Felton & Loth (2001) studied bubbles in the 400–1200 μm range in a vertical boundary layer. They were interested in the dynamics of large spherical bubbles injected in an upward flowing channel. The mean void fraction profiles were obtained, but not the instantaneous concentration fields. Moreover, the mean flow was in the same direction as the buoyancy, so the rise velocity was not considered. Results from well-resolved direct numerical simulations of a bubbly turbulent boundary layer became available in the literature only very recently in the work of Ferrante & Elghobashi (2004). They performed direct numerical simulations of a spatially developing flat-plate turbulent boundary layer laden with microbubbles. They found that the bubbles induce compressibility of the carrier fluid velocity field and that this is the leading-order term in the modification of the dynamics of the turbulent boundary layer laden with microbubbles. They compared different orientations of the plate relative to gravity and determined that it is compressibility, and not buoyancy, that creates a secondary flow normal to the wall. This flow away from the wall is responsible for the lifting of the streamwise turbulent structures that produce ejections and sweeps. Their interpretation is that this mechanism can explain the decrease in the rate of production of turbulent kinetic energy and the reduction of the skin friction by microbubble injection.

In this paper, we describe an experimental investigation of the behaviour of microbubbles injected into a turbulent boundary layer developing along a surface-piercing vertical flat plate. In particular, the study is focused on the effect of buoyancy

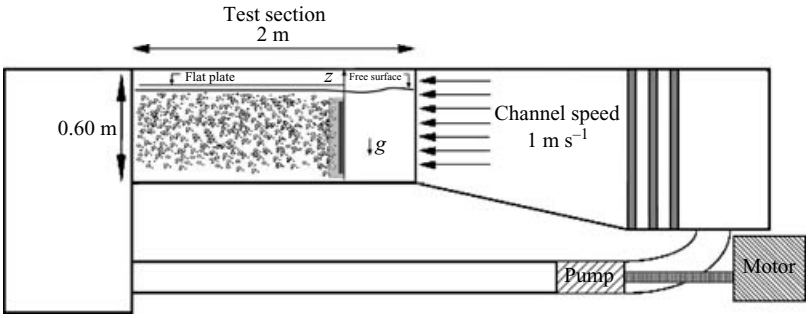

FIGURE 1. Recirculating water channel.

on the flow dynamics and the description of the complex flow developing as the bubbly turbulent boundary layer interacts with the free surface. The outline of the paper is as follows. In § 2, the facility and measurement techniques used in the experiments are described. Measurements of the three components of the velocity and the bubble concentration field, along with visualizations of the flow near the free surface, are shown in § 3. The analysis of the experimental data is given in § 4, describing the mechanism for vorticity generation associated with the presence of the bubbles. Finally, the conclusions of this work are summarized in § 5.

2. Experimental set-up

The experiments were carried out in a recirculating water channel with a capacity of roughly $5\,\mathrm{m}^3$. The free stream in the channel has a maximum speed of $1\,\mathrm{m\,s}^{-1}$. The test section is 2 m long and has a square cross-section of $0.6\,\mathrm{m} \times 0.6\,\mathrm{m}$. The channel has a series of grids and honeycombs, followed by a contraction, to assure that fluctuations originating at the pump are damped out before the flow reaches the test section. The underlying turbulent intensity of the free stream is very low, less than 0.5 %. A Plexiglas plate was cut to dimensions $2\,\mathrm{m} \times 0.6\,\mathrm{m} \times 0.0127\,\mathrm{m}$ and mechanized so that it could be placed vertically inside the test section of the water channel. A bubble injector, described below, was attached to the plate at the leading edge so that the bubbles were introduced inside the boundary layer, at the beginning of its development. The injector also served as a tripping mechanism necessary for the boundary layer to go through the transition to turbulence within the channel test section. Once positioned inside the test section, the flat plate extended horizontally through the entire length of the test section and vertically from the bottom of the channel to well above the free surface. Thus, the flat plate pierces the surface, originating a corner type flow at the junction of the solid plate and the free surface. A sketch of the facility is shown in figure 1.

The experiments require the injection of very small bubbles, with a Sauter mean diameter $d_{32} \approx 200\,\mu\mathrm{m}$, in very large numbers so that the volume fraction is significant in order to study the influence of the bubbles in the underlaying turbulent carrier flow, $\phi \approx 10^{-3}$. The injector consists of an aluminium NACA 0012 profile with a longitudinal cavity machined along its leading edge. The cavity is closed with a porous plate through which compressed air, supplied from the side of the hydrofoil, is bubbled into the incoming flow. To further reduce the bubble size, ethanol microjets are directed at the porous plate along the leading edge of the hydrofoil so that the contact angle of the growing bubbles is increased, making it easier for bubbles

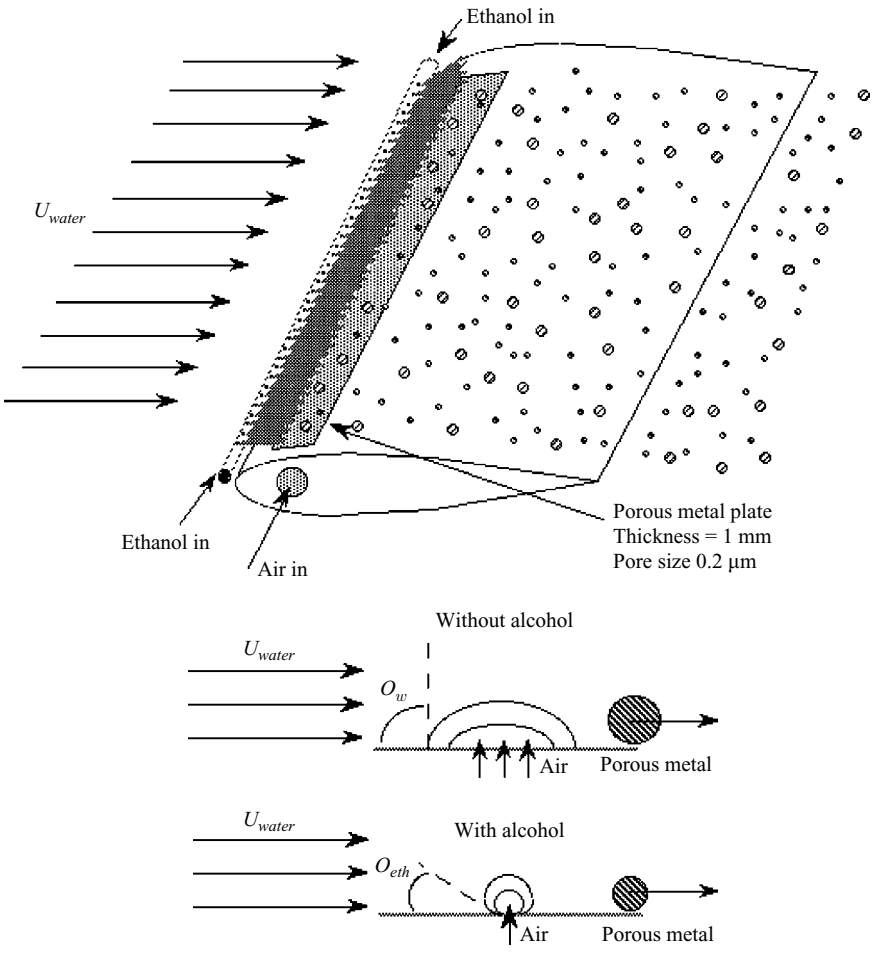

FIGURE 2. Sketch of the bubble generator and the diameter reduction mechanism.

to detach from the plate. Essentially, the volume to cross-sectional area ratio is decreased and, since drag depends on the area exposed to the incoming fluid, bubbles with smaller volume are formed. A schematic of the device and the mechanism of size reduction is shown in figure 2. The volume of alcohol injected is very small, approximately $1\,\mathrm{ml\,s^{-1}}$, and so its effect on the bulk properties of the carrier fluid is negligible (initial volume fraction smaller than 10^{-3}).

A spatially uniform distribution of bubbles is created by the injector at the leading edge of the plate. The size distribution of bubbles injected at different depths can be seen in figure 3. This initial uniformity disappears as the bubbles interact with the turbulent structures of the boundary layer and the gravitational field. The initial bubble void fraction at the injection point is very large, of the order of 5 %, but quickly decreases as the largest bubbles created by the injector, which carry a large part of the volume, rise to the surface and disappear. Thus, the void fraction inside the turbulent boundary layer, measured a few boundary thicknesses downstream of the injection, is in the range $o(10^{-5}) - o(10^{-3})$, and bubble–bubble interactions can be considered negligible.

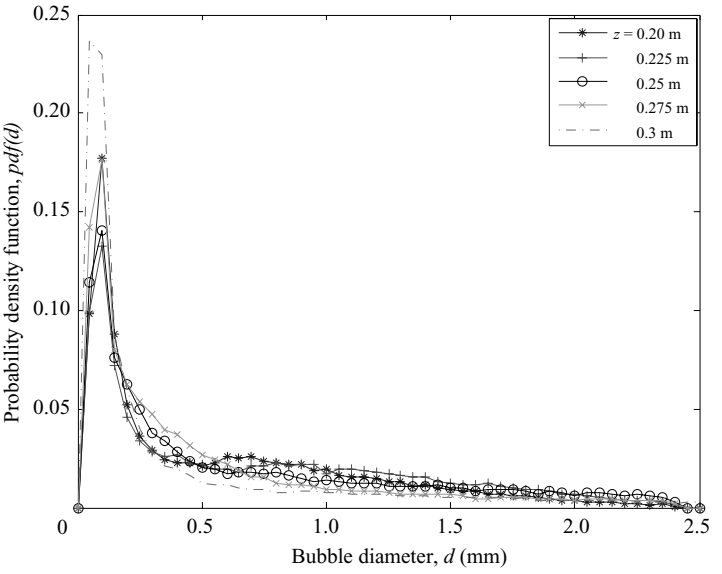

FIGURE 3. Bubble diameter distribution at injection.

2.1. *Flow-visualization technique*

Flow visualizations were obtained using a Canon Optura digital video recorder and stored in Mini-DV format tape. Except in a few cases where ambient light was used, in most instances the flow was illuminated by a laser plane created using a continuous Coherent I-70C Ar^+ laser and a Lincoln Laser rotating mirror operating at 500 Hz. The plane could be oriented to illuminate a vertical slice of the flow, perpendicular to the free-stream flow, as indicated in figure 4(*a*). The camera was situated at the end of the channel, looking into the test section through a Plexiglas window in the channel's endwall. The laser plane could also be positioned horizontally, perpendicular to the flat plate, as shown in figure 4(*b*), cutting across the boundary layer. In this case, the camera was located under the test section looking up, through the transparent channel floor. Finally, the flow was also illuminated by a vertical laser plane parallel to the flat plate and the free stream in the test section. To do this, the rotating mirror was located under the test section and the camera looked horizontally into the test section through the transparent walls (see figure 4*c*).

2.2. *Bubble size measurements*

A high-resolution (1008×1008 pixels) Kodak ES 1.0 digital camera was used to characterize the bubble size distribution and the concentration, as well as the velocity field. The location of the bubbles was determined from images of the light reflected by the bubbles in the flow. Using NIH image-processing software, the images were made binary and analysed. By thresholding the data with different light intensities, the noise due to multiple reflections, current leakage from saturated pixels or microlens spreading can be rejected. However, strict thresholds reject small bubbles which create dim reflections in the images. The sensitivity of the measurements to the threshold was systematically analysed and found to be negligible in the range used in our experiments. Using this image-processing technique, the location of the bubble centroid was computed and stored. Information on the preferential accumulation of bubbles obtained with this method is presented in § 3.3.

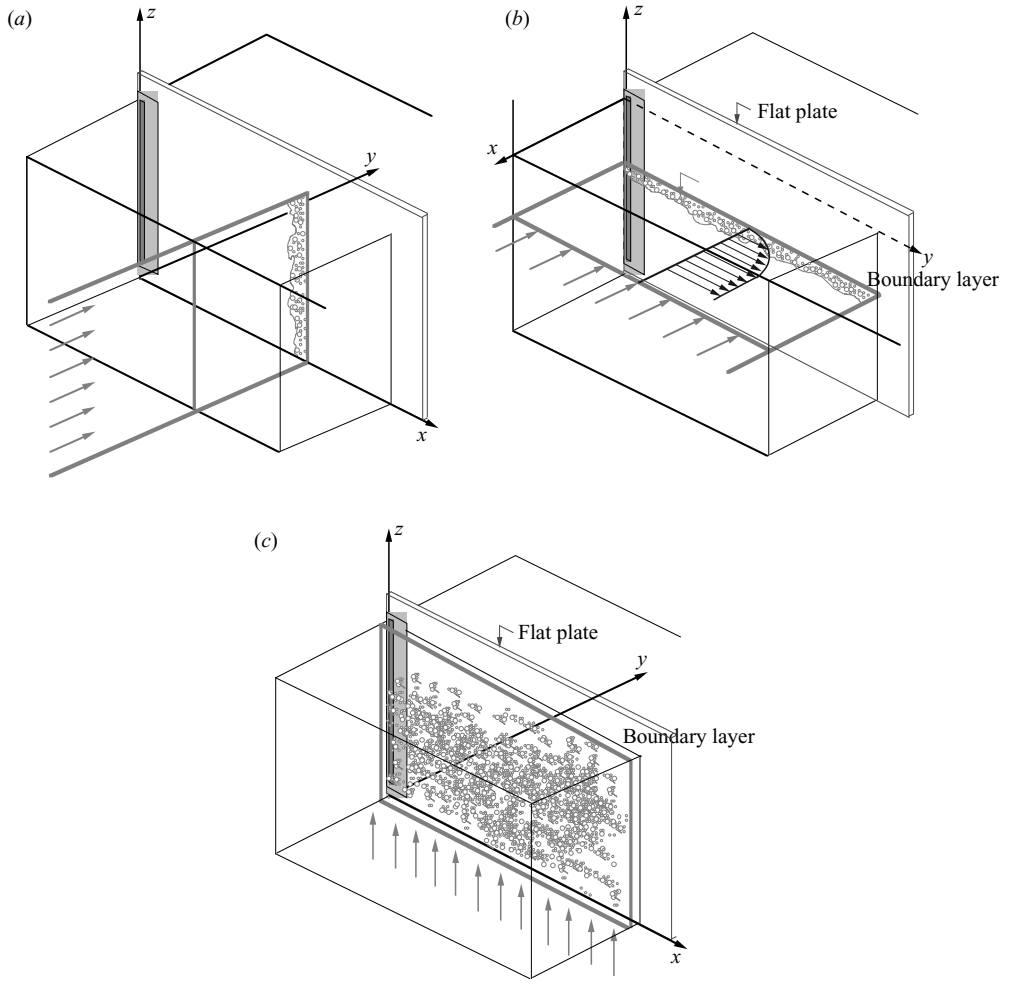

FIGURE 4. Sketch of the laser plane orientations (shown by arrows) for flow visualizations.

Statistics of the bubble diameter distribution were obtained from attenuation images taken with the digital camera described above. A source of collimated light was placed opposite to the camera, on the other side of the test section. Thus, the light propagated across the test section and was scattered by the bubbles in the boundary layer. The camera captured the light deficit created by the bubbles with respect to the bright background. A typical image is shown in figure 5. The camera was focused on a point 15 mm from the plate, where the bubble number density was highest, and set to a small aperture, $f/32$. With a 200 mm macro lens located at 1 m from the plate, a 2 cm depth of field was achieved, encompassing a large fraction of the boundary-layer width. A background image was captured, in the absence of bubbles, and subtracted from the bubble image to minimize the errors due to uneven illumination conditions. The outcome of this substraction was then thresholded and processed to extract the area and location of the bubbles. The equivalent diameter was computed from the cross-sectional area, assuming the bubbles were spherical.

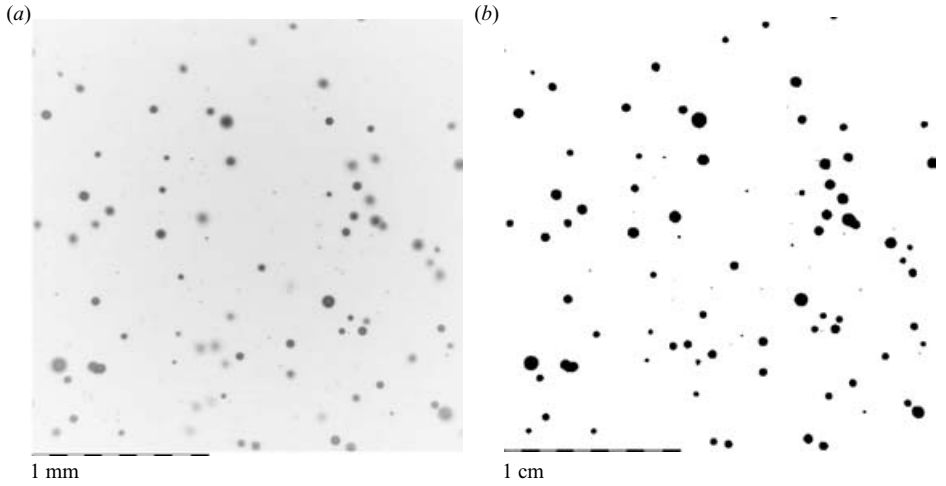

FIGURE 5. Typical image of the flow used to determine the bubble diameter distribution.

2.3. *Velocity measurements*

Measurements of the velocity were obtained from images of the flow illuminated by the laser plane in the two configurations shown in figures 4(*b*) and 4(*c*). The frequency of the rotating mirror was synchronized with the time exposure of the camera to ensure that two sweeps of the laser beam would be captured in each frame. Also, an *a priori* evaluation of the velocities to be measured was carried out, so that the displacement of the bubbles between sweeps would be large enough to minimize the experimental error. This, together with the high spatial resolution of the images ensured a low uncertainty of the measurements. An estimate for a single velocity measurement can be computed as:

$$\frac{\Delta x}{x} = \frac{0.5\,\text{pixel}}{2.5 \times 10^4\,\text{pixel}\,\text{m}^{-1} \times 1.25 \times 10^{-3}\,\text{s} \times 0.6\,\text{m}\,\text{s}^{-1}} \approx 2.75\,\%. \tag{2.1}$$

The values of the different terms in (2.1) are given by a 25 000 pixels m^{-1} optical magnification, an exposure time of 1.25 ms and a free-stream velocity of 60 cm s^{-1}. The uncertainty in the location of the bubble centroid in the image is the leading cause of experimental error in this type of measurement. The contribution of the uncertainty in the timing between images to the total velocity error is negligible because of the high precision of the rotating mirror system (< 0.002).

In the first set of measurements, the flow was illuminated with a horizontal streamwise laser plane, normal to the flat plate and parallel to the free surface. The streamwise and wall-normal velocity components were extracted, by both particle image velocimetry (PIV) and particle tracking velocimetry, from the images. The plane was positioned at a depth $z = 0.28$ m from the free surface, deep enough that the boundary layer was not affected by free-surface effects. The second set of measurements consists of streamwise and vertical velocities obtained from images of the flow illuminated by a laser plane parallel to the flat plate and located at different distances from the plate. The camera was focused on a small region, approximately 0.04 m $\times$ 0.04 m, at the same depth as the first set of measurements. The interaction between the three components of the velocity could then be analysed.

Images were taken at two downstream distances from the leading edge, $x = 0.36$ m and $x = 0.94$ m, both were far enough downstream for the boundary layer to have transitioned into a fully turbulent state and the characteristics of the flow were independent of the tripping mechanism. Since the free-stream velocity dominates the formation of the bubbles at the injector, as well as their convection along the plate inside the boundary layer, the void fraction and Reynolds number at a given location are both functions of the channel mean velocity. By taking measurements at different locations within the boundary layer we were able to change the Reynolds number and the void fraction independently.

Velocity measurements were obtained using a commercial PIV software package (TSI Insight) as well as an in-house particle-tracking algorithm. The results from both techniques were very consistent, with the particle tracking providing better results in low void fraction cases, owing to the larger spatial resolution and number of realizations, whereas the PIV provided better results in high void fraction situations, owing to the larger number of bubbles per interrogation window and the difficulties of the tracking algorithm in identifying bubble pairs in these cases. A very large number of images, $o(10^3)$, were collected for each flow condition and an ensemble-average was computed from all the measurements. The spatial resolution for the PTV was about 50 μm, while for the PIV it was close to 800 μm (using a spot size of 32 pixels with a 50 % overlap).

3. Experimental results

3.1. *Visualizations of the flow at the boundary layer–free surface intersection*

A top view of the flow facility is shown in figure 6. In this picture of the water channel, the flow moves from top to bottom and the surface-piercing flat plate, located in the middle of the channel's test section with the bubbles being injected on its left-hand side, can be seen at the right-hand edge of the picture. The free surface presents a typical Kelvin wave, with a set of capillary waves radiating from it, produced by the presence of the plate. A foamy line can be observed starting at the leading edge of the plate, separating from it and becoming parallel to the plate at a certain distance. This is, as explained in § 4, the surface signature of a submerged streamwise vortex that develops near the juncture of the plate and the free surface.

Figure 7 shows a horizontal cross-section of the bubbly boundary layer, as well as some features of the outer juncture flow. The flow is from right to left. The boundary layer is tripped by the bubble injector and the bubbles themselves making the bubbly boundary layer considerably thicker than the single-phase case for an equivalent Reynolds number based on the distance downstream. As it develops, bubbles diffuse inside the boundary layer but, as can be clearly seen from figure 8, they remain confined to it, not diffusing into the free stream. Some surface features are made visible by multiple scattering of the laser light from the regions where bubbles accumulate. A close up of this view is shown in figure 8. Non-uniformities in the bubble concentration field, resulting from the interaction of the bubbles with the turbulent structures that are present inside the boundary layer, are apparent.

A snapshot of the flow illuminated by a vertical laser plane, perpendicular to the free-stream flow, is shown in figure 9. The most outstanding feature of this flow is the existence of a streamwise vortex located at a certain distance and depth with respect to the plate. This large coherent structure has circulation of the same sign as the outer vortex described in single-phase juncture flows (Sreedhar & Stern 1998;

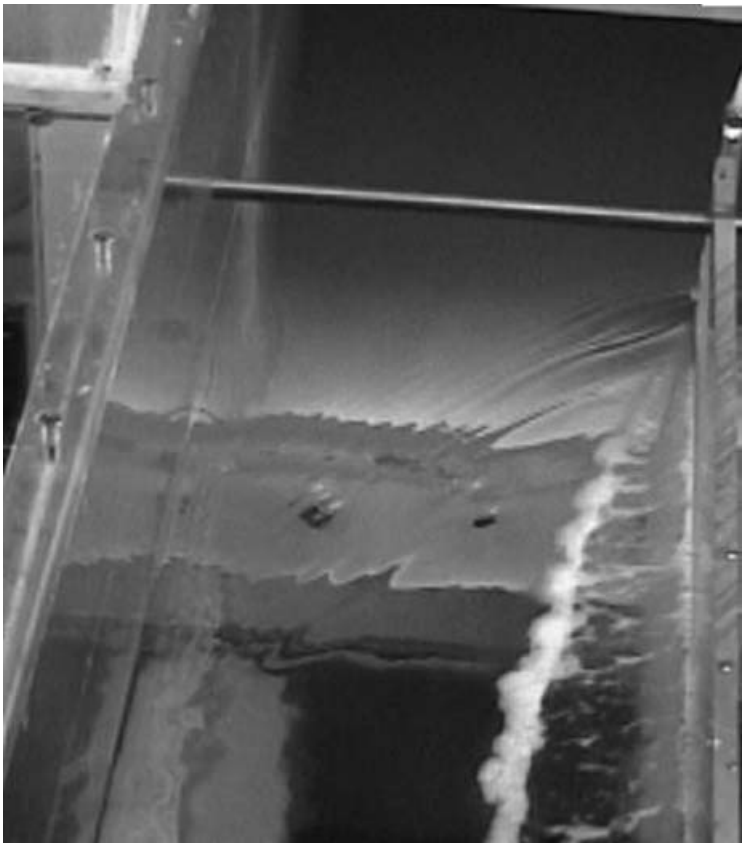

FIGURE 6. Overall view of the flow facility.

Grega, Hsu & Wei 2002); however, its strength is much larger. A source of streamwise vorticity associated with the presence of the bubbles is described in the § 4.

To further clarify the origin of the strong coherent vortex seen in the previous figure, and to determine its relationship with the vorticity that has been described in single-phase juncture flows, we performed visualizations with fluorescein injected on both sides of the plate. Figure 10(*a*) shows how the fluorescein introduced into the flow near the bubbly side of the plate is convected upwards and entrained by the vortex, alongside the bubbles. When fluorescein is introduced into the flow on the other side of the plate where there are no bubbles (figure 10*b*), it diffuses slowly owing to random fluctuations, with no visible coherency in the flow.

3.2. *Velocity measurements*

The streamwise velocity profiles measured are shown in figure 11. They were found to be very similar to the well-known profiles from single-phase turbulent boundary layers (Klebanoff 1955). The existence of a logarithmic region was confirmed for all cases studied, with the local bubble void fraction going up to 10^{-3}. The non-dimensional profiles corresponding to those plotted in figure 11 are displayed in figure 12, normalized using viscous scales. Measurements within the viscous and buffer layer were restricted by the spatial resolution of the images, $\delta^+ < 1$ pixel.

Unlike the streamwise component, the wall-normal velocity profile measured was very different from the single-phase boundary layer. Figure 13 shows profiles of the

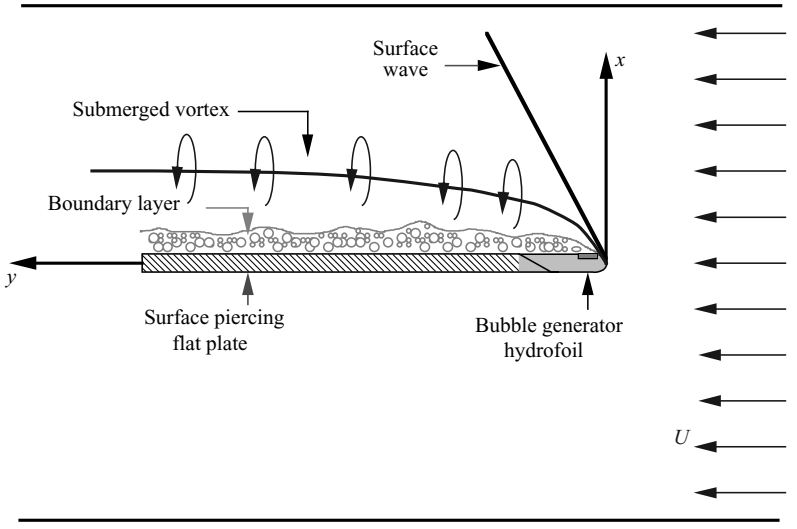

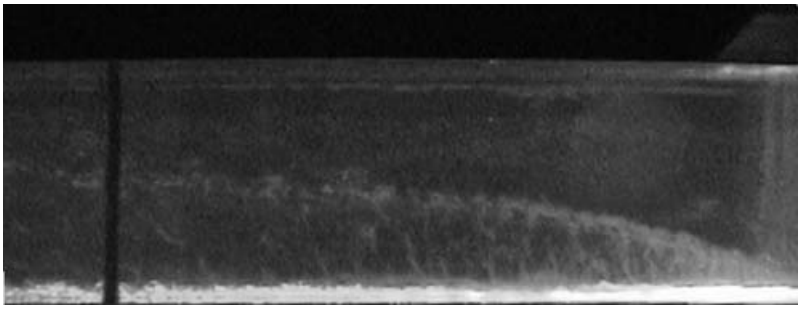

FIGURE 7. Horizontal section. General view.

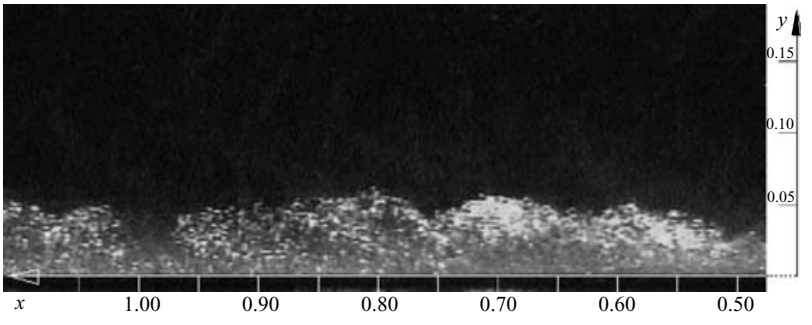

FIGURE 8. Horizontal section, close up. Instantaneous bubble concentration field.

velocity normal to the wall, for different values of the Reynolds number and void fraction. It can be seen that the flow normal to the wall does not vary with the Reynolds number, but rather it is strongly dependent on the bubble void fraction in the boundary layer, becoming stronger as the void fraction increases. This hypothesis is supported by figure 14 in which the wall-normal velocity is plotted against the distance from the wall, both normalized with viscous scales. The lack of a collapse of

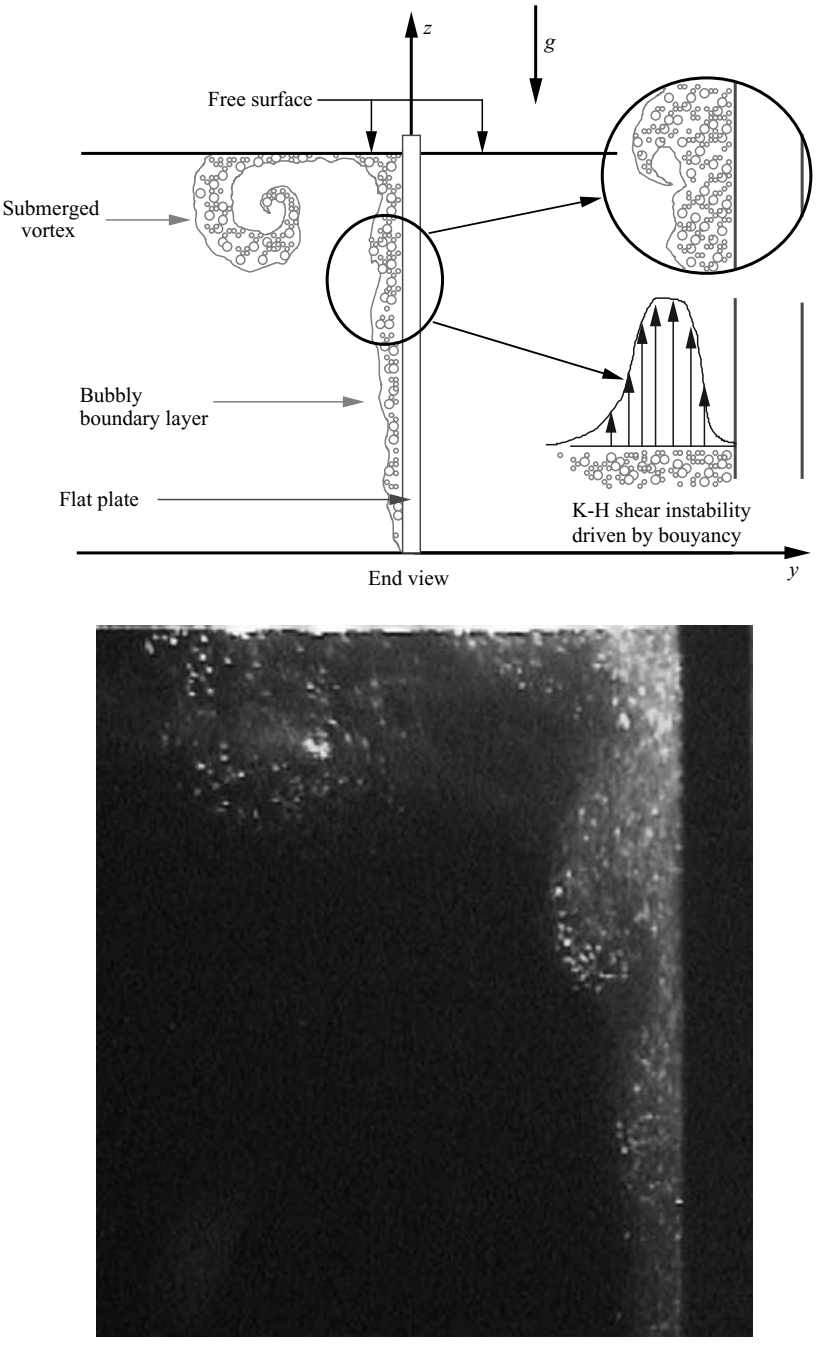

FIGURE 9. Vertical section. General view.

both curves seems to indicate that this secondary flow, normal to the wall, is caused by the presence of the bubbles, not by the dynamics of the turbulence near the wall.

Measurements of both the vertical velocity of the bubbles and the carrier flow were conducted at the same depth and distance downstream as the previous ones. A vertical laser plane, parallel to the flat plate, was positioned at three different distances

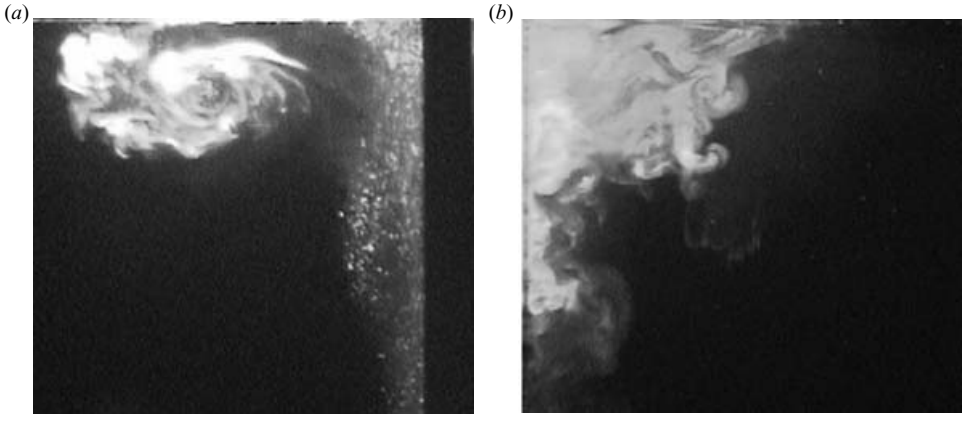

FIGURE 10. Fluorescein visualizations. (*a*) Strong coherent structure on the bubbly side. (*b*) No coherency on the single-phase side.

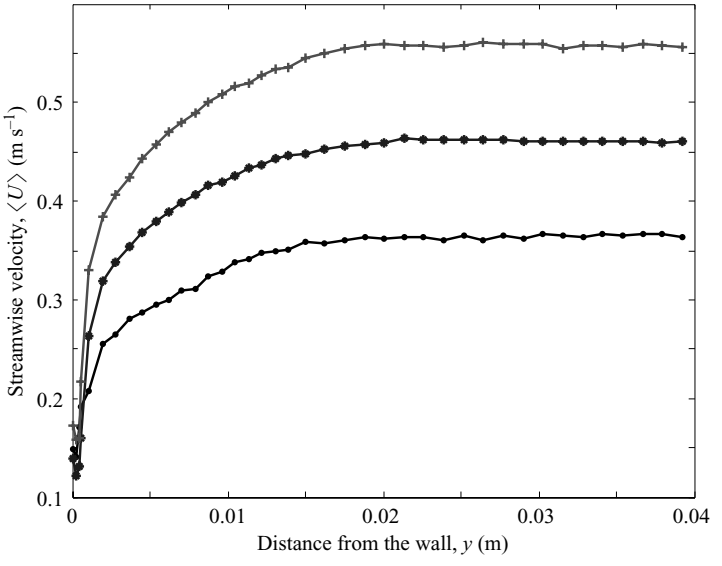

FIGURE 11. Streamwise velocity profiles. Dimensional quantities.

from the wall, namely at $y = 8$, 13, 18 mm ($y/\delta \approx 0.4,\ 0.7,\ 0.95$). These three positions are located in the three different subregions determined by the wall-normal velocity profile. That is, in the region where the normal velocity is away from the wall, at the line where the normal velocity is zero, and in the region where the normal velocity is towards the wall. In this way, the relation between the secondary flow normal to the wall and the vertical flow induced by the buoyancy of the bubbles can be confirmed. The vertical velocity profile of the carrier flow is plotted in figure 15.

The number density and diameter of the bubbles were also measured. The distribution of bubbles is plotted in figure 16 against the distance from the wall, measured by the boundary layer-width. It can be seen that the number density of bubbles is not uniform within the boundary layer. It grows from almost zero near the wall to a very sharp maximum, and decays back to zero as the distance from the wall grows. The volume-averaged diameter of the bubbles is also plotted against the wall distance, in

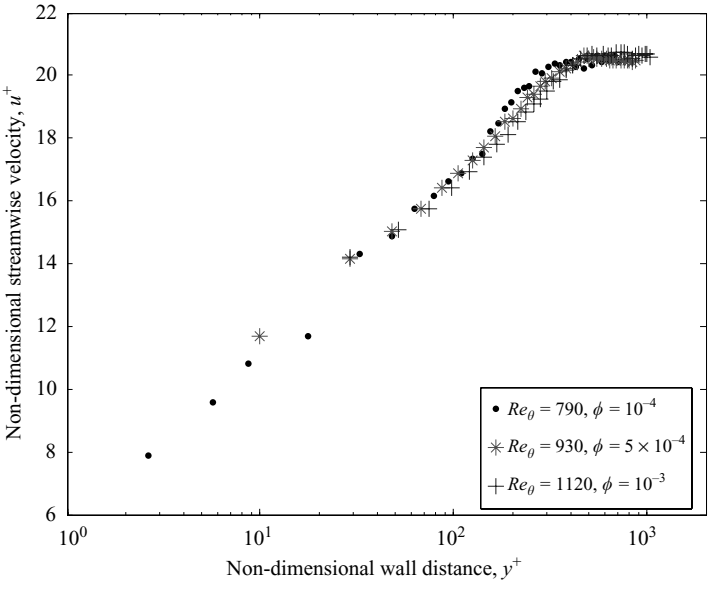

FIGURE 12. Non-dimensional streamwise velocity profiles.

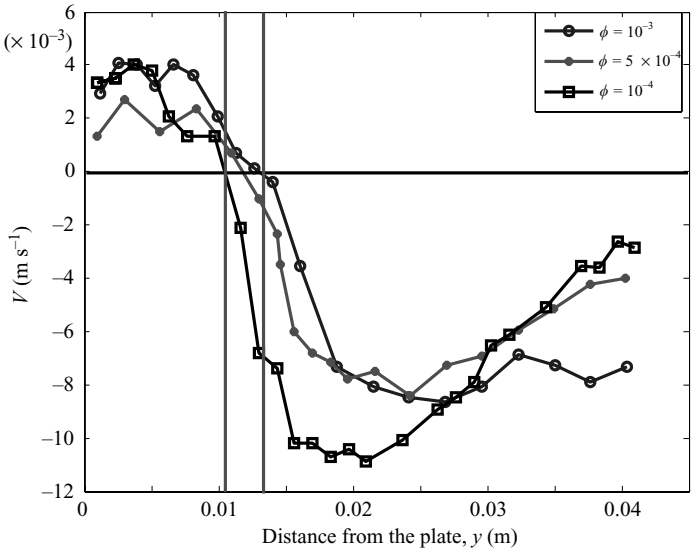

FIGURE 13. Wall-normal velocity profiles.

figure 17. Significant size segregation occurs inside the boundary layer. The average diameter is very small, of the order of 100 μm, in the region closest to the wall. It grows significantly, up to a value of 200 μm in the intermediate region, corresponding to the location of the maximum of the vertical velocity. Then, the average bubble size reduces quickly as we move away from the wall, past the maximum of the vertical velocity profile.

The vertical velocity of the bubbles was measured at three locations, corresponding to the three regions described above. These measurements were then averaged for bubbles with equal diameter and the rise velocity of the bubbles computed by this

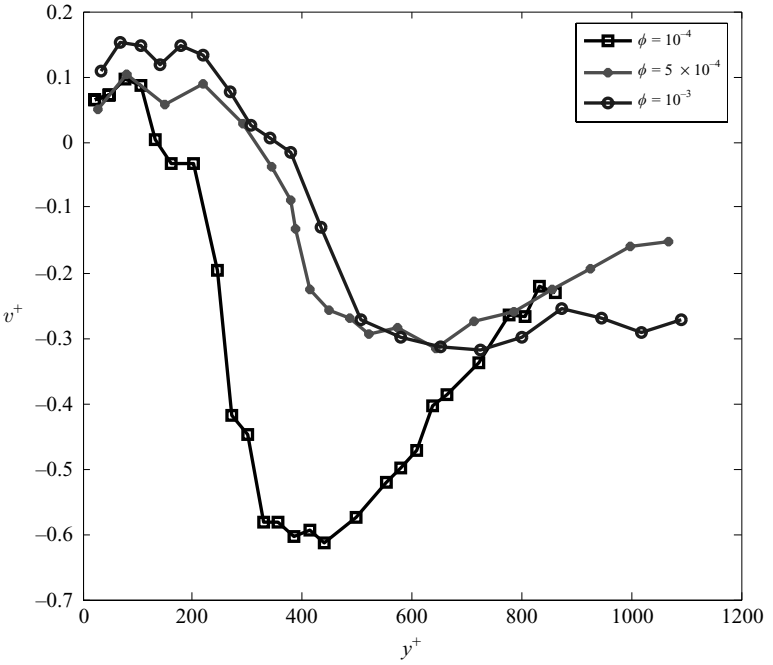

FIGURE 14. Wall-normal velocity profiles. Non-dimensionalized using viscous scaling.

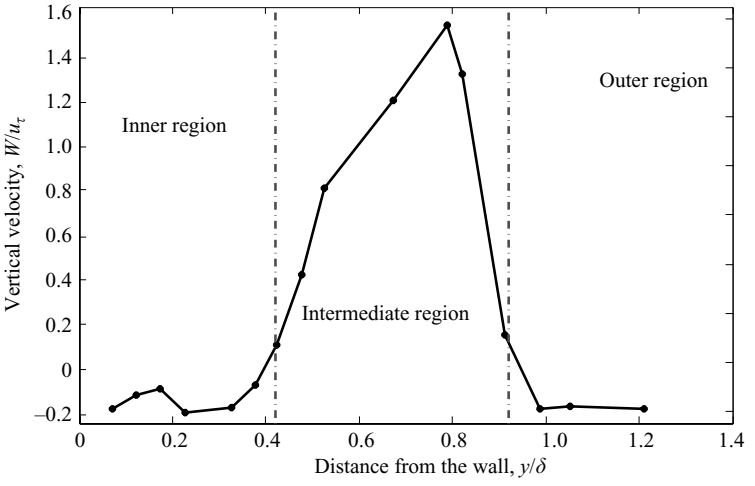

FIGURE 15. Vertical velocity profile for the carrier flow.

method is compared in figure 18 against the rise velocity of microbubbles in still fluid measured by Detsch (1989). It is clearly observed that the behaviour of the bubbles is different depending on their position with respect to the wall. The rise velocity of bubbles inside the inner region is similar to the one measured in still fluid. It is slightly enhanced for the smallest bubbles and slightly reduced for the largest bubbles. Inside the intermediate region, where the vertical velocity of the carrier fluid reaches its maximum, the rise velocity is significantly enhanced for bubbles of all sizes. For bubbles in the outer region, however, rise velocity is equal to or even smaller than

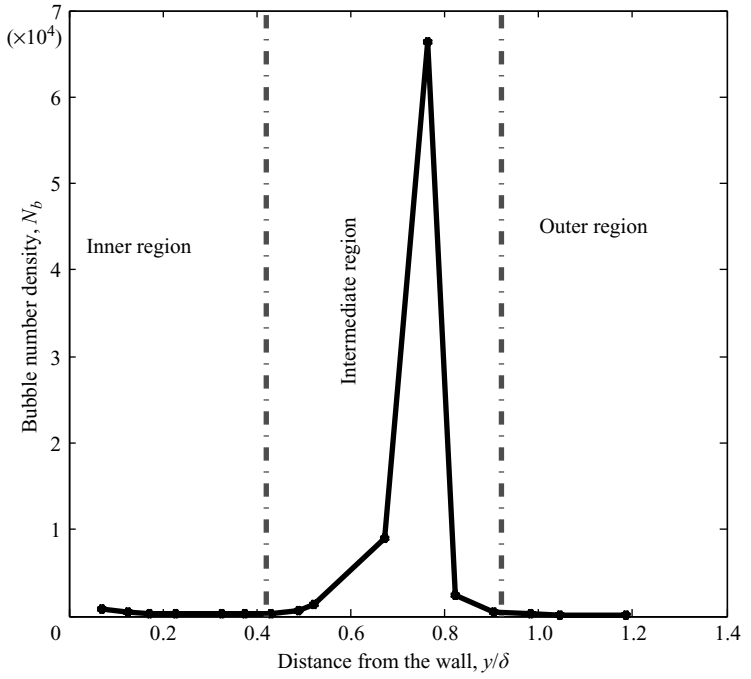

FIGURE 16. Bubble number density as a function of the distance from the wall.

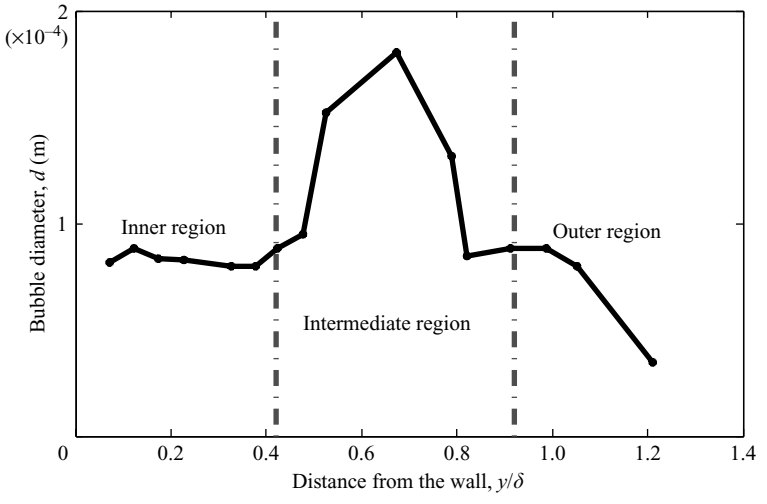

FIGURE 17. Volume averaged diameter of the bubbles as a function of the distance from the wall (d_{30}).

the still fluid value. In particular, the largest bubbles present in this region have a reduction in the rise velocity of up to 50 %.

3.3. *Bubble accumulation due to the turbulence*

The positions of the bubble centroids were determined by the image-processing technique described in § 2.1. This information was evaluated by different algorithms to characterize how the instantaneous bubble concentration field correlated with

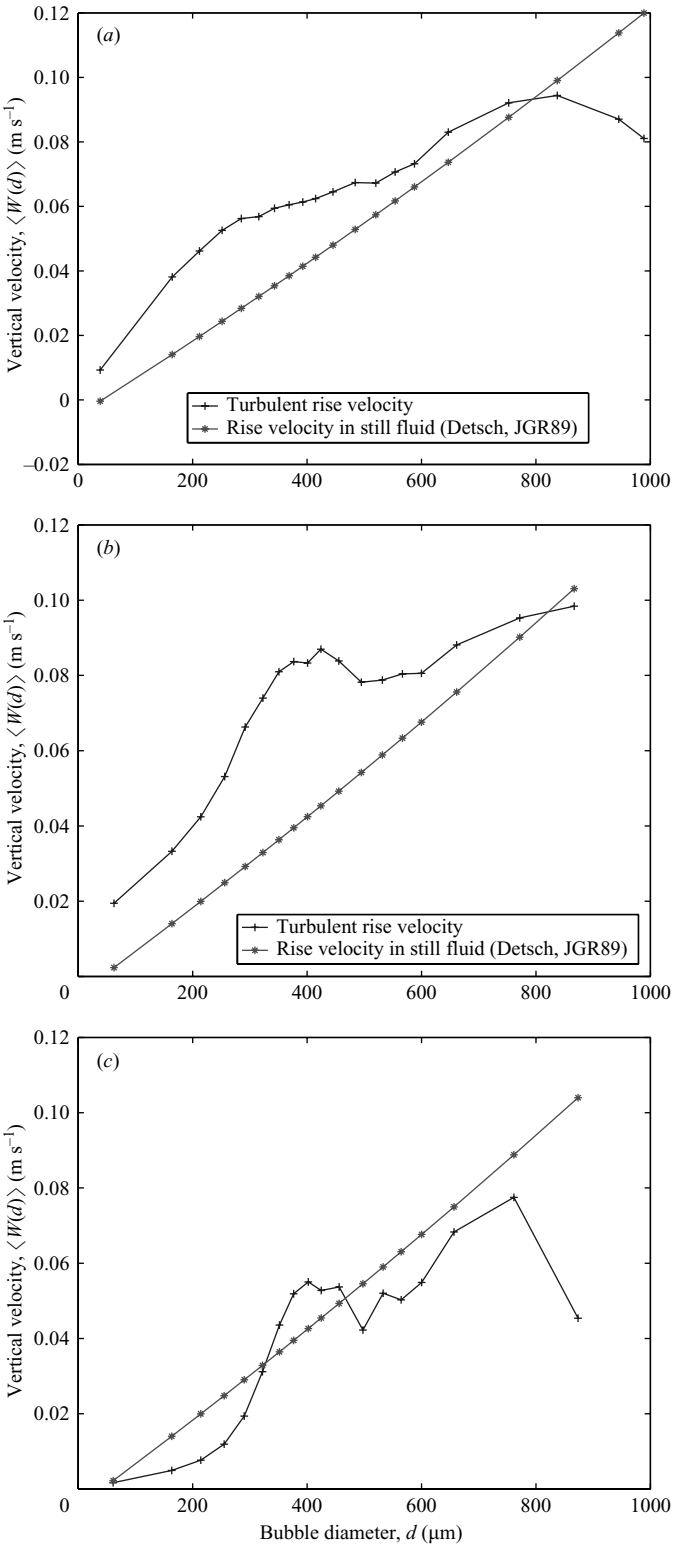

FIGURE 18. Average rise velocity of the bubbles as a function of their diameter, conditioned to the position inside the boundary layer. (*a*) $y = 8$ mm (inner region), (*b*) $y = 13$ mm (rising region), (*c*) $y = 18$ mm (outer region).

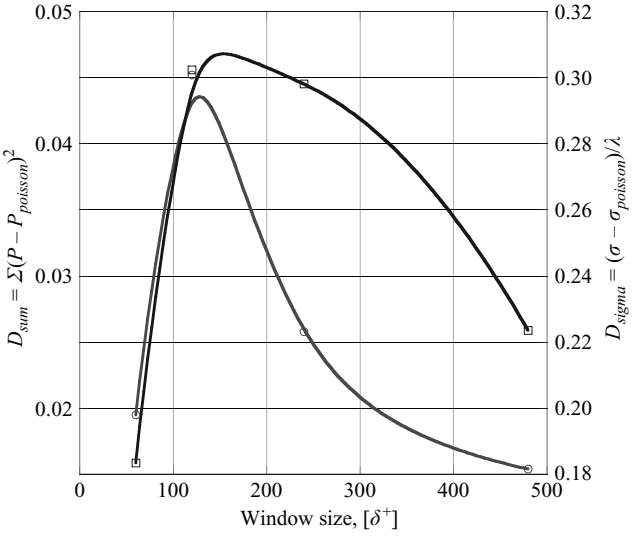

FIGURE 19. Bubble accumulation as a function of the length scale. Indicators defined in equations (3.2) and (3.3). (i) $D_{sigma} = (\sigma - \sigma_{poisson})/\lambda$; (ii) $D_{sum} = \Sigma(P - P_{poisson})^2$.

the turbulent structures present in the flow. The algorithm used to identify bubble clustering by the turbulence consists of the following steps. First, each image is divided into square windows of a certain size. The number of bubbles within each of these non-overlapping windows is counted and recorded. With the information corresponding to all the windows covering every image taken under a given condition, we can compute the density function for the probability of finding a number of bubbles $P(n_b)$ in each one of these windows. If the bubbles were passive scalars, their spatial concentration due to the random stirring of the turbulence would correspond to a Poisson distribution.

$$P_{poisson}(n) = \frac{\mathrm{e}^{-\lambda}\lambda^n}{n!}, \tag{3.1}$$

where λ is the mean number of particles per window, N_b/N_w. By comparing the observed probability density function with the theoretical Poisson PDF resulting from a purely random process, it is then possible to quantify how the bubble concentration field deviates from randomness. By repeating this algorithm for different window sizes, the dependency of this deviation on the length scale can be determined. Two different ways of comparing the PDFs were employed to quantify the extent of bubble clustering in the boundary layer. Their definitions, due to Wang & Maxey (1993*a*) and Fessler, Kulick & Eaton (1994) respectively, are as follows:

$$D_{sum} = \sum_{n=1}^{N_b} (P(n_b) - P_{poisson}(n_b))^2, \tag{3.2}$$

$$D_{sigma} = \frac{\sigma - \sigma_{poisson}}{\lambda}, \tag{3.3}$$

where $P(n)$ is the probability of finding n bubbles in a window, and $\sigma_{poisson}$ is the standard deviation of the Poisson distribution.

The values of these quantities, computed for many different window sizes are plotted in figure 19. Both indicators of preferential accumulation reach a maximum

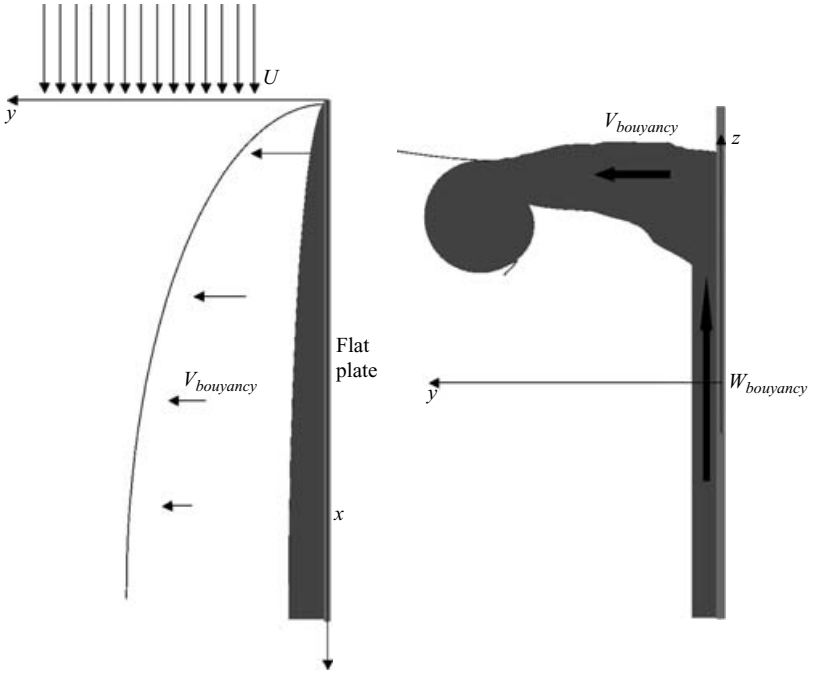

FIGURE 20. Schematic of the flow rising along the boundary layer and, at the surface, away from the plate.

value for a length scale of 100 wall units, indicating that this is the flow scale at which bubble accumulation is most significant. The two quantities plotted tend to zero for very small and very large scales, as expected, as accumulation due to turbulence must disappear for scales smaller than the smallest scale in the flow, viscous length, or larger than the largest turbulent scale, the boundary-layer thickness.

4. Analysis and discussion of the results

4.1. *Flow characteristics at the boundary layer–free surface intersection*

The fluid inside the boundary layer rises along with the bubbles and, once it reaches the free surface, moves away from the plate, by continuity (see figure 20). This surface flow carries the bubbles around before they have time to reach the surface and burst open. The effect of the bubble size on this surface flow away from the plate can be seen in figure 21. For the same bubble void fraction, the smaller bubbles are more effective at entraining fluid from the boundary layer, resulting in a larger flow rate induced at the surface and a wider angle separating the free stream and the surface flow.

The vertical velocity profile has been measured and shown to have two shear layers that will become unstable and roll up. In figure 22, which is a close-up of figure 9, we can see the roll-up of the outer shear layer subject to a Kelvin–Helmholtz/Rayleigh–Taylor mixed type instability. This instability causes the positive streamwise vorticity generated by the velocity and density gradients to accumulate in large coherent vortices. In this figure, we can also identify, by the presence of the streamwise billows at the interface between the bubbly layer and the free stream, the source of vorticity

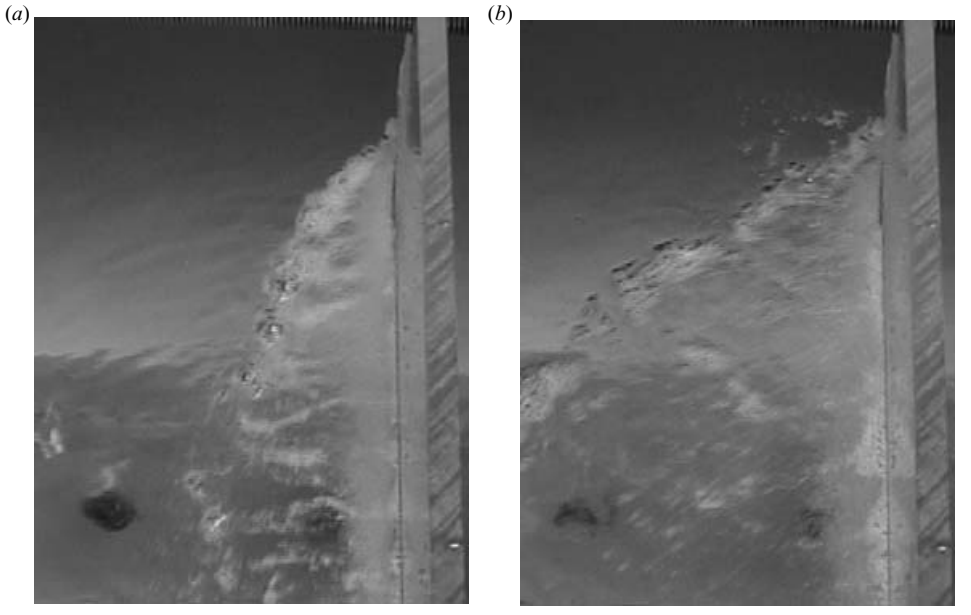

FIGURE 21. Effect of the bubble size on the induced surface flow. (*a*) Sauter mean diameter = 450 μm. (*b*) Sauter mean diameter = 250 μm.

that ends up in the coherent vortex described above. Note that these billows have the same sense of rotation as the vortex, whereas there should be another shear layer very close to the wall, that generates vorticity of opposite sign. A sketch of the mechanism for this instability is shown in figure 9. The density gradient, and the vertical velocity gradient associated through gravity, are sources of streamwise vorticity in the flow, which do not exist in the single-phase boundary layer. The streamwise vorticity, resulting from the vertical shear, couples with the vertical vorticity present in the boundary layer as a result of the horizontal shear (see figure 23). This coupling leads to a complex pattern of tilted vortex lines, a sketch of which is found in figure 24, that resembles those found by Thorpe (1985) and Atsavapranee & Gharib (1997) in stratified mixing layers inclined around two perpendicular axes. The vorticity generated in the boundary layer is advected upwards by the buoyant flow. Once they reach the surface, the vortex lines becomes parallel to it and reconnect in the form of a strong coherent streamwise vortex that positions itself at a certain depth and angle with the plate. These white filaments are made visible in figures 6 and 7 by the accumulation of bubbles near the cores.

The submerged streamwise vortex formed by the reconnection of all those vortex lines entrains the surface flow generated by buoyancy and thus serves as a demarcation line that divides the boundary-layer flow, laden with bubbles, from the free stream that is unaffected by the presence of the bubbles. To corroborate this hypothesis, fluorescein was injected into the boundary layer. Figure 25 shows the boundary-layer fluid, marked with fluorescein for this visualization, rising to the surface and being entrained by the vortex. Thus, the vortex growth and its separation from the plate is explained by the entrainment of the bubbly flow which carries positive vorticity. The vortex core captures bubbles from the boundary layer as they come near the surface. These bubbles remain near the vortex core for long times, coalescing until they are

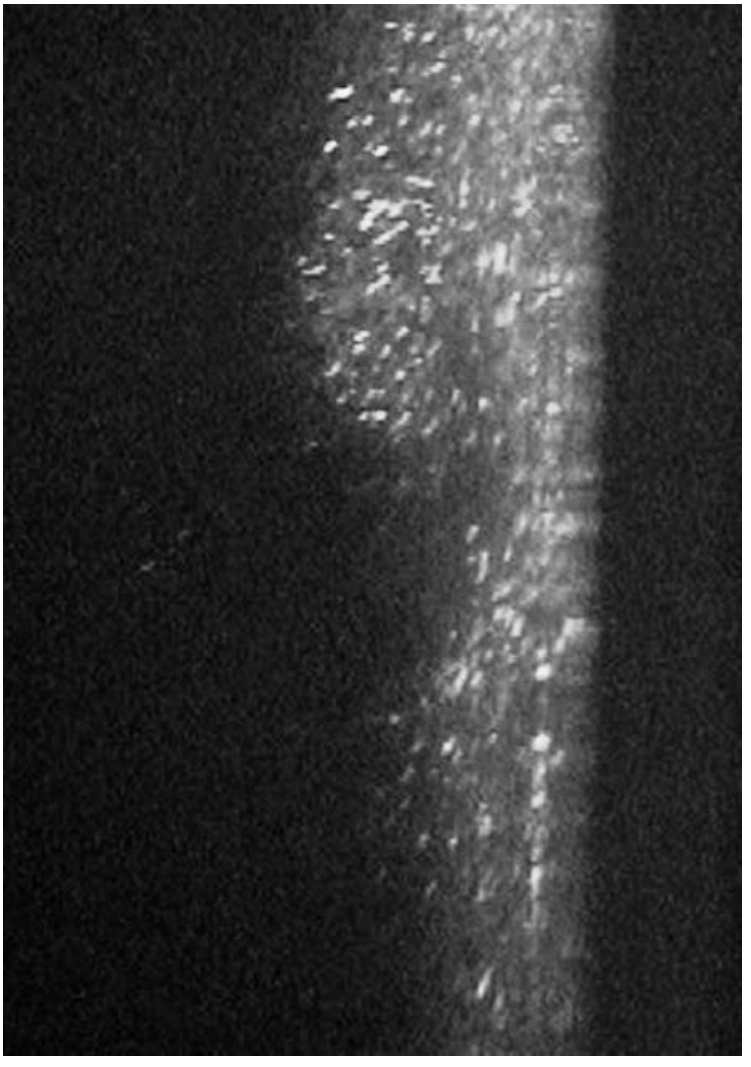

FIGURE 22. Vertical section. Close-up of the Kelvin–Helmholtz-type billows present in the boundary layer.

large enough to escape the vortex and rise to the surface. At the surface, these large bubbles create a foamy pattern that helps to locate the position of the vortex from the surface.

The presence of bubbles in the boundary layer introduces important modifications to the dynamics of this flow, which has been described in the previous section. In this section, the velocity and concentration fields measured are interpreted in the light of the accepted mechanisms of interaction between microbubbles and turbulent flows.

Buoyancy introduced by the bubbles induces an upwards moving velocity in the carrier fluid. This vertical component of the velocity must necessarily go to zero at the wall and at the free stream, thus two shear layers of opposite sign are created. These shear layers become unstable, originating streamwise vorticity. The bubbles are attracted towards the core of these vortices by pressure forces. At the same time,

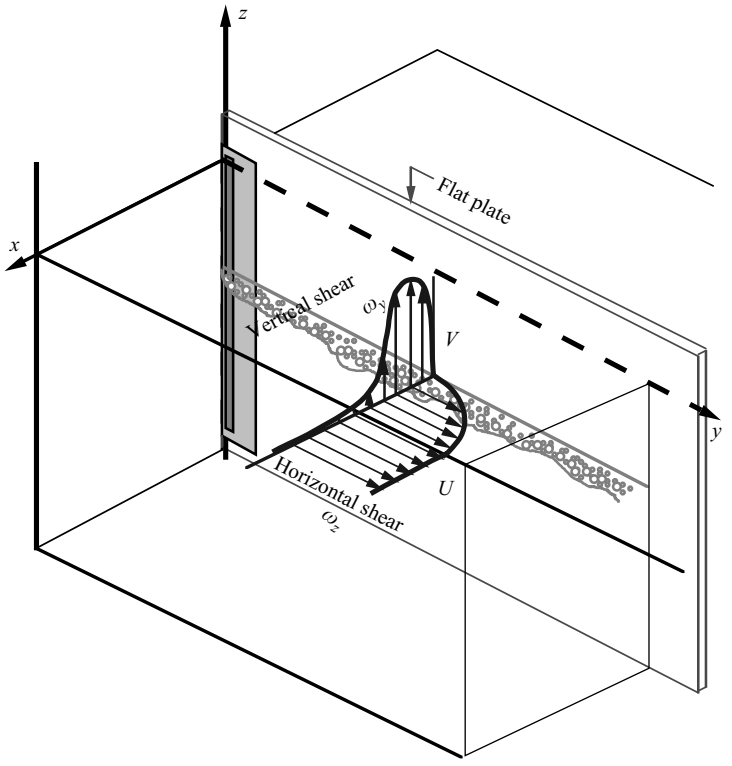

FIGURE 23. Schematic of the horizontal and vertical velocity profiles.

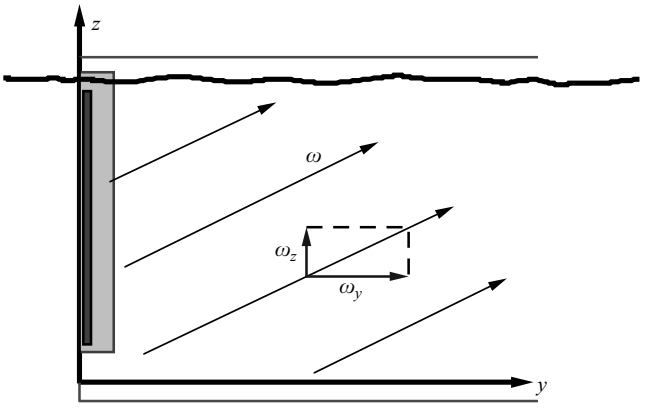

FIGURE 24. Schematic of the vortex lines pattern resulting from the coupling of the boundary-layer vorticity with the buoyancy-induced streamwise vorticity.

owing to the horizontal shear imposed by the wall, bubbles are subjected to a lift force in the direction of increasing streamwise velocity (Magnaudet & Eames 2000). The bubbles which are originally injected at the wall, are pulled away from it by a combination of lift and pressure forces. These forces preferentially drive the larger bubbles away from the wall towards the edge of the boundary layer where the shear is smaller. The resulting size segregation reinforces the shear in the upwards moving flow

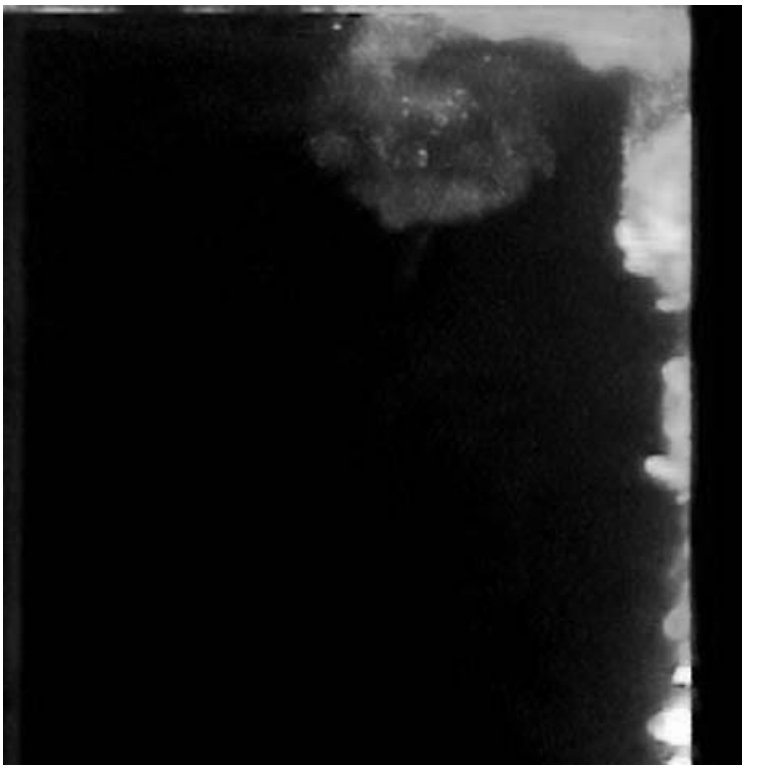

FIGURE 25. Vortex entraining boundary-layer fluid. Fluorescein visualization.

due to buoyancy which in turn strengthens the streamwise vortices, feeding energy back into the accumulation process. The outcome of this self-sustaining mechanism is a vertical velocity profile with a sharp peak, a strong segregation of bubbles by size with the larger bubbles accumulating in a central region within the boundary layer, and a convergent flow normal to the wall moving away from the wall close to it and towards the wall at the outer edge of the boundary layer. There is also a modification of the streamwise velocity resulting from the last secondary flow mentioned above.

4.2. *Streamwise velocity*

The parameters of the logarithmic law that fits the velocity profile were found to depend on the local void fraction. An offset from the wall was introduced as a new parameter in an effort to find a universal fit to the streamwise velocity profile in the logarithmic layer for the different values of Reynolds number and bubble void fraction. The physical mechanism by which the bubbles modify the buffer layer close to the wall cannot yet be described, but it is hypothesized that the secondary wall-normal flow, that is greatly enhanced by the presence of the bubbles, thickens the low-speed region, displacing the log-layer away from the wall proportionally to the relative volume occupied by the bubbles. The results can be seen in figure 26. A systematic dependency of the wall offset with the local void fraction was found, and it is shown in figure 27. As the lack of an independent measurement of the wall shear stress makes it impossible to estimate a best fit (DeGraaf & Eaton 2000), the

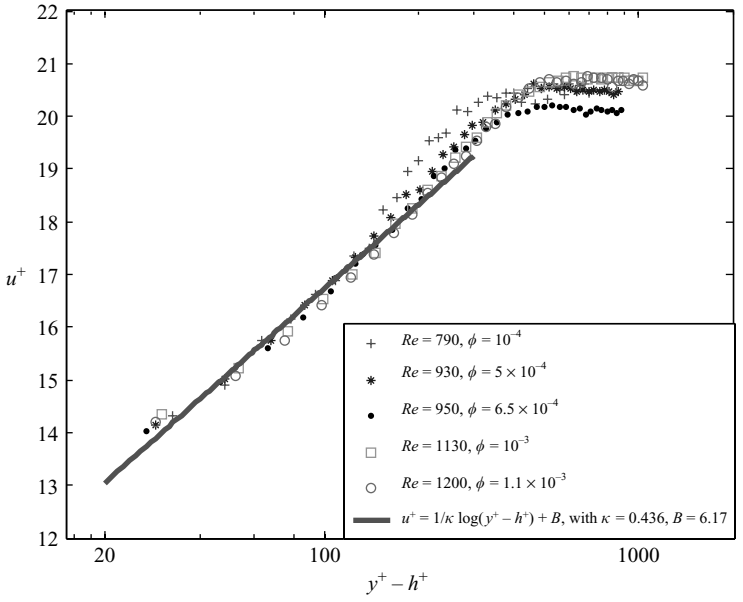

FIGURE 26. Logarithmic fit to the normalized streamwise velocity profiles, using a wall offset that is dependent on the bubble void fraction.

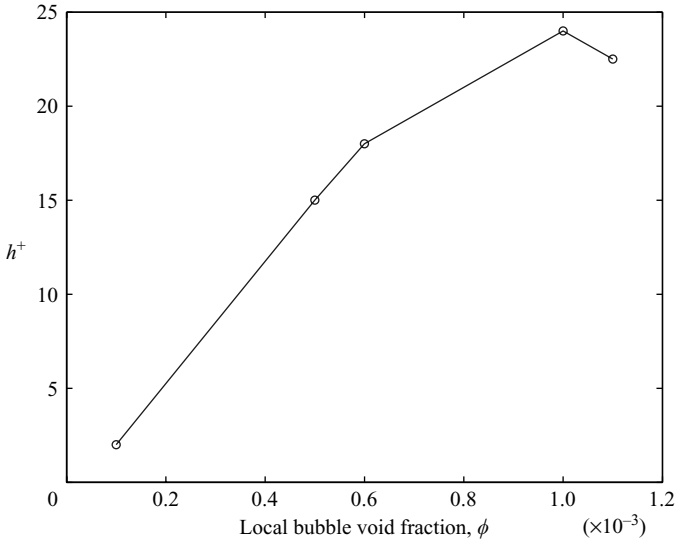

FIGURE 27. Offset from the wall of the logarithmic layer, as a function of the local bubble void fraction averaged across the boundary-layer thickness.

value of the wall offset was computed for two sets of parameters from single-phase boundary-layer studies (Coles 1956; Zagarola, Perry & Smits 1997). Thus, the two parameters κ and B were fixed *a priori* and the fitting process provided estimates of the wall shear stress and the log-layer offset from the wall. In both cases, the offset was consistently dependent on the bubble void fraction, increasing as the void fraction increases. This simple model provides a way of relating the velocity profile of

the bubbly boundary layer with the well-known logarithmic profile of the single-phase turbulent boundary layer. Thus, the transport of bubbles can be computed without the need to take into account the interaction of the bubbles with the carrier flow.

4.3. *Secondary flows*

A secondary flow, two orders of magnitude smaller than the channel mean velocity is established within the boundary layer. The characteristics of this flow normal to the wall, unlike the single-phase case, consist of a small region near the wall where the flow is moving away from the wall, and a larger region, in the outer zone of the boundary layer, in which there is a relatively strong flow towards the wall. The flow in these two regions converges to a line, located between 200 and 400 wall units, for the Reynolds numbers and void fractions studied. By continuity, these converging flows must go out of the plane and, as shown by the vertical velocity measurements described below, they do flow upwards. The position of the maximum vertical velocity must, then, be correlated with the location of the line of zero wall normal velocity, as observed in figure 15.

There is a strong size segregation inside the boundary layer, which is shown in figure 17. In this figure, we can see the strong variation of the diameter in three regions, that resembles the vertical velocity profile. The strong inhomogeneity in the distribution of the buoyancy, coupled by the zero vertical velocity boundary conditions at the wall and in the free stream, leads to the development of the highly sheared vertical velocity profile, seen in figure 15. The entrainment of carrier fluid by the buoyantly rising region induces the secondary flow normal to the wall that was found in figure 13. These secondary flows explain the existence of the three regions within the boundary layer with two zones of strong vertical shear. In the inner region closer to the wall, the vertical velocity is very low, restricted by the presence of the wall, the wall-normal velocity is positive, that is away from the wall, and the bubble average size is small. The intermediate region has a very large vertical velocity, with two areas of high shear of opposite sign, the wall-normal velocity is very low and the average size of the bubbles is maximum. Finally, the outer region has very low vertical velocity, asymptotically going to zero as it approaches the free stream, the wall-normal component of the velocity is directed towards the wall and the bubble size and number density are smallest. The extent of these three regions is determined by the dynamics of the turbulent boundary layer, the Reynolds number, and by the effect of the bubbles in the flow, the void fraction. Although the variation of the turbulent scales present in the experiment was not large enough to make any definite statements about the scaling of these three regions, we hypothesize that the largest number of bubbles, and those of larger sizes, accumulate at the edge of the boundary layer, in the intermittent viscous super layer where large vortices create the strongest pressure forces. According to Murlis, Tsai & Bradshaw (1982), this superlayer has mean position at 0.8δ, with standard deviation 0.15δ, in good agreement with the measured location of the rising region shown in figure 15.

The average rise velocity of the bubbles is different in each of the three regions within the boundary layer. As shown in figure 18(*b*), the bubbles in the intermediate region, where the entrained fluid has maximum vertical velocity, rise faster than they would in still fluid. This is in apparent contradiction to the hindering of the rise velocity of bubbles by turbulence that has been reported from numerical simulations (Maxey *et al.* 1997; Mazzitelli *et al.* 2003), as well as experiments (Poorte & Biesheuvel 2002; Aliseda & Lasheras 2006), in homogeneous isotropic unbounded turbulent flows. Obviously, this contradiction is simply due to the effect of convection. The non-zero

value of the local vertical velocity of the carrier fluid adds up to the rise velocity of these bubbles that can be computed by a balance between viscous drag, which depends on the slip velocity, and buoyancy.

$$\left.\begin{aligned} &\frac{\pi}{6}d^3(\rho_b-\rho_f)\boldsymbol{g}=\frac{\pi}{4}d^2C_D\rho_f|\boldsymbol{v}-\boldsymbol{u}|(\boldsymbol{v}-\boldsymbol{u}); \quad C_D\approx\frac{24}{Re},\\ &\frac{\pi}{6}d^3(\rho_b-\rho_f)\boldsymbol{g}=\frac{\pi}{4}d^2\frac{24\nu_f}{|\boldsymbol{v}-\boldsymbol{u}|d}\rho_f|\boldsymbol{v}-\boldsymbol{u}|(\boldsymbol{v}-\boldsymbol{u}); \quad \frac{\rho_b}{\rho_f}\ll 1,\\ &v_z=u_z+\frac{d^2g}{36\nu_f}, \end{aligned}\right\} \tag{4.1}$$

where v_z is the bubble vertical velocity, u_z is the carrier fluid vertical velocity, d is the bubble diameter and ν_f is the kinematic viscosity of the carrier fluid. The simplifying assumption of $C_D=24/Re$ has been made for illustrative purposes only. The rise velocity in still fluid with which the measured bubble velocity is compared in figure 18 was experimentally determined (Detsch 1989), and takes into account non-zero Reynolds number and surfactant effects.

In both the inner and outer regions, the effect of the turbulence on the rise velocity of the bubbles was found to be strongest for the largest bubbles. The rise velocity of the small bubbles correlates only with the vertical convective velocity of the carrier fluid. In the inner region, the rise velocity is slightly increased owing to the small upwards velocity of the fluid, whereas in the outer region the rise velocity is unaffected, corresponding to the zero mean vertical velocity in this region. The rise velocity of the large bubbles is reduced in both cases owing to the turbulent fluctuations (see figure 18*a*, *c*). This reduction can be also glimpsed by looking at the difference between the vertical velocity of the bubbles in the intermediate region and the one in still fluid. The increase in the bubbles rise velocity comes out to be much smaller than the peak velocity of the carrier fluid shown in figure 15, approximately $2\,\mathrm{cm\,s^{-1}}$ *vs.* $4\,\mathrm{cm\,s^{-1}}$. This difference can be interpreted as a reduction of the rise velocity due to turbulence.

5. Conclusions

The dynamics of a turbulent boundary layer laden with microbubbles have been studied experimentally. The configuration chosen for the study was a vertical surface-piercing flat plate, with the air bubbles injected at the leading edge into the horizontal water flow. In this way, the bubbles were confined to the boundary layer, as they were convected by the carrier flow and rise under the effect of buoyancy. The presence of a relatively high void fraction of bubbles inside the boundary layer introduced a source of momentum perpendicular to the free stream, generating secondary flows in the vertical and wall normal directions. The presence of these secondary flows had a very significant effect on the transport of the bubbles, as well as on the statistics of the mean carrier flow.

The logarithmic law, characteristic of single-phase turbulent boundary layers, was found to be still valid in the bubble-laden turbulent boundary layer. It was found that a logarithmic fit that preserves the canonical values of the constants described in the single-phase literature could be used, with the addition of a new constant. This constant, which depends on the bubble void fraction, represents an offset in the distance from the wall that is necessary for the logarithmic law to apply.

The secondary flows induced by buoyancy inside the boundary layer, created three regions with distinct values of the bubble number density, average diameter and rise

velocity. The inner region is characterized by the presence of flow normal to the wall and away from it, coupled with low positive values of the vertical velocity. It was found to be populated by a low number of relatively small bubbles, $d_{30} = 100\,\mu$m, which had their rise velocity enhanced compared to the value in still fluid. The intermediate region presents a maximum of the vertical velocity, corresponding to the region where the wall normal flow is zero. The largest bubbles accumulate almost exclusively in this region, resulting in a marked increase of the average diameter, $d_{30} = 200\,\mu$m, and a very large increase of the bubble number density. As a result of the large vertical velocity of the carrier fluid, the rise velocity of bubbles of all sizes in this region is significantly increased. Finally, in the outer region, the vertical component of the velocity is essentially zero and the wall normal component is strongly negative, that is, directed towards the wall. This region has the smallest bubble number density and average diameter, $d_{30} = 80\,\mu$m, resulting from the difficulty of the bubbles to diffuse into a region where both the wall normal velocity and the vertical shear are negative. Unlike in the previous two cases, the rise velocity of the bubbles in this region is reduced owing to the turbulence and the zero value of the carrier fluid vertical velocity.

The instability of the strongly sheared vertical velocity profile coupled with the presence of a density gradient normal to the hydrostatic pressure gradient, acted as a source of streamwise vorticity. As a result of the coupling of the streamwise vorticity with the vertical vorticity present in the boundary layer, there was a complicated pattern of tilted vortex lines, which rose to the surface and were convected away from the wall and reconnected into a strong coherent streamwise vortex that dominates the junction flow. This vortex, which originated at the leading edge of the plate, lay at a depth and distance from the wall that were dependent on the Reynolds number of the flow and the bubble void fraction.

This work was supported by the ONR through grant N00014-05-1-0121. A. A. is indebted to the La Caixa Foundation for a Graduate Fellowship.

REFERENCES

Aliseda, A. & Lasheras, J. 2006 The effect of homogeneous isotropic turbulence on the rise velocity and concentration field of micro bubbles. *Phys. Fluids* (submitted).

Atsavapranee, P. & Gharib, M. 1997 Structures in stratified plane mixing layers and the effect of cross shear. *J. Fluid Mech.* **342**, 53–86.

Coles, D. 1956 The law of the wake in a turbulent boundary layer. *J. Fluid Mech.* **1**, 191–226.

Crowe, C., Chung, J. & Troutt, T. 1988 Particle mixing in free shear flows. *Prog. Energy Combust. Sci.* **14**, 171–194.

DeGraaf, D. & Eaton, J. 2000 Reynolds number scaling of the flat-plate turbulent boundary layer. *J. Fluid Mech.* **422**, 319–346.

Detsch, R. 1989 Small air bubbles in reagent grade water and seawater 1. Rise velocities of 20 to 1000 μm diameter bubbles. *J. Geophys. Res.* **96** (C5), 8901–8906.

Druzhinin, O. & Elghobashi, E. 1998 Direct numerical simulations of bubble-laden turbulent flows using the two fluid formulation. *Phys. Fluids* **10**, 685–697.

Eaton, J. & Fessler, J. 1994 Preferential concentration of particles by turbulence. *Intl J. Multiphase Flow* **20** (Suppl.), 169–209.

Felton, K. & Loth, E. 2001 Spherical bubble motion in a turbulent boundary layer. *Phys. Fluids* **13**, 2564–2577.

Ferrante, A. & Elghobashi, S. 2004 On the physical mechanisms of drag reduction in a spatially developing turbulent boundary layer laden with microbubbles. *J. Fluid Mech.* **503**, 345–355.

Fessler, J., Kulick, J. & Eaton, J. 1994 Preferential concentration of heavy particles in turbulent channel flow. *Phys. Fluids* **6**, 3742–3749.

Grega, L., Hsu, T. & Wei, T. 2002 Vorticity transport in a corner formed by a solid wall and a free surface. *J. Fluid Mech.* **465**, 331–352.

Klebanoff, P. 1955 Characteristics of turbulence in a boundary layer with zero pressure gradient. *NACA Tech. Rep.* 1247.

Lance, M. & Bataille, J. 1991 Turbulence in the liquid phase of a uniform bubbly air–water flow. *J. Fluid Mech.* **222**, 95–118.

Magnaudet, J. & Eames, I. 2000 The motion of high Reynolds-number bubbles in inhomogeneous flows. *Annu. Rev. Fluid Mech.* **32**, 659–708.

Marie, J., Moursali, E. & Trang-Cong, S. 1997 Similarity law and turbulence intensity profiles in a bubbly boundary layer at low void fractions. *Intl J. Multiphase Flow* **23**, 227–247.

Maxey, M. & Riley, J. 1983 Equation of motion for a small rigid sphere in a nonuniform flow. *Phys. Fluids* **26**, 883–889.

Maxey, M., Patel, B., Chang, E. & Wang, L. 1997 Simulations of dispersed turbulent multiphase flow. *Fluid Dyn. Res.* **20**, 143–156.

Mazzitelli, I., Lohse, D. & Toschi, F. 2003 On the relevance of the lift force in bubbly turbulence. *J. Fluid Mech.* **488**, 283–313.

Merkle, C. & Deutsch, S. 1992 Microbubble drag reduction in liquid turbulent boundary layers. *Appl. Mech. Rev.* **45**, 103–127.

Moursali, E., Marie, J. & Bataille, J. 1995 An upward turbulent bubbly boundary layer along a vertical flat-plate. *Intl J. Multiphase Flow* **21**, 107–117.

Murlis, J., Tsai, H. & Bradshaw, P. 1982 The effect of convex surface curvature on turbulent boundary layers. *J. Fluid Mech.* **122**, 13–56.

Panidis, T. & Papailiou, D. 2000 The structure of two-phase turbulence in a rectangular channel: an experimental study. *Intl J. Multiphase Flow* **26**, 1369–1400.

Poorte, R. & Biesheuvel, A. 2002 Experiments on the motion of gas bubbles in turbulence generated by an active grid. *J. Fluid Mech.* **461**, 127–154.

Rightley, P. & Lasheras, J. 2000 Bubble dispersion and interphase coupling in a free shear flow. *J. Fluid Mech.* **412**, 21–59.

Segre, G. & Silberberg, A. 1962 Behaviour of macroscopic rigid spheres in Pouiseuille flow. *J. Fluid Mech.* **14**, 115–157.

Spelt, P. & Biesheuvel, A. 1997 On the motion of gas bubbles in homogeneous isotropic turbulence. *J. Fluid Mech.* **336**, 221–244.

Sreedhar, M. & Stern, F. 1998 Prediction of solid/free-surface juncture boundary layer and wake of a surface-piercing flat plate at low Froude number. *Trans ASME* I: *J. Fluids Engng* **120**, 354–362.

Sridhar, G. & Katz, J. 1995 Drag and lift forces on microscopic bubbles entrained by a vortex. *Phys. Fluids* **7**, 389–399.

Taylor, G. 1921 Diffusion by continuous movements. *Proc. R. Soc. Lond.* A **20**, 196–211.

Thorpe, S. 1985 Laboratory observations of secondary structures in Kelvin–Helmholtz billows and consequences for ocean mixing. *Geophys. Astrophys. Fluid Dyn.* **34**, 175.

Tio, K., Laheras, J., Gañán Calvo, A. & Liñán, A. 1993 The dynamics of bubbles in periodic vortex flows. *Appl. Sci. Res.* **51**, 285–290.

Wang, L. & Maxey, M. 1993*a* Settling velocity and concentration distribution of heavy particles in homogeneous isotropic turbulence. *J. Fluid Mech.* **256**, 27–68.

Wang, L. & Maxey, M. 1993*b* The motion of microbubbles in a forced isotropic and homogeneous turbulence. *Appl. Sci. Res.* **51**, 291–296.

Zagarola, M., Perry, A. & Smits, A. 1997 Log laws or power laws: the scaling in the overlap region. *Phys. Fluids* **9**, 2094–2100.